Synthesis of g-C₃N₄/BiOI/BiOBr heterostructures for efficient visible-light-induced photocatalytic and antibacterial activity

Bingkun Liu[1] · Xiaole Han[1] · Yu Wang[1] · Xin Fan[1] · Zhuoyue Wang[1] · Jingtao Zhang[2] · Hengzhen Shi[1]

Abstract

Visible-light-driven g-C₃N₄/BiOI/BiOBr composite photocatalysts were successfully synthesized by a facile deposition precipitation method. The as-prepared samples have been characterized by X-ray diffraction (XRD), X-ray photoelectron spectroscopy (XPS), field emission scanning electron microscopy (FESEM), transmission electron microscopy (TEM) and ultraviolet–visible absorption spectroscopy (UV–vis). The photocatalytic experiments indicate that the g-C₃N₄/BiOI/BiOBr composites possess enhanced photocatalytic activity towards the degradation of methyl orange (MO), and killing *Escherichia coli*. Photoluminescence (PL) spectra reveal that the introduction of *g*-C₃N₄ could efficiently promote the separation efficiency of photo-induced charge carriers in the composites. The radical trapping experiment and ESR analysis confirmed that the active species $\cdot O_2^-$, h⁺ and ·OH are the reactive oxygen species in the photocatalytic process. Our results suggest that the g-C₃N₄/BiOI/BiOBr composite photocatalysts can be used in water treatment of degrading the organic pollutants and killing the water bacteria at the same time.

1 Introduction

Since the last century, energy shortage and environmental pollution are major challenges for sustainable environmental development. As a kind of clean and renewable energy, solar energy has made a rapid progress in research. In recent years, photocatalysis technology based on semiconductor materials has gained great attention, which can use solar energy to degrade organic pollutants and disinfection [1–3]. So far, TiO₂ has been demonstrated as an effective photocatalyst in environmental areas [4–6]. However, the wide band gap limits their photoactivity to the visible region, making them inefficient for solar light applications. Thus, the exploration and application of novel visible-light-driven (VLD) photocatalysts remains a most essential challenge.

Graphitic carbon nitride (*g*-C₃N₄), a polymeric metal-free semiconductor with a band gap of about 2.70 eV, has been recently focused on the photocatalytic field because of its non-toxicity, abundance and stability [7–9]. Unfortunately, the photocatalytic efficiency of bare *g*-C₃N₄ is largely limited by a high recombination rate of the photogenerated electron–hole pairs. Therefore, many strategies have been proposed to overcome these drawbacks of *g*-C₃N₄, including the construction of a porous structure [10], metal or nonmetal deposition [11, 12], and semiconductor couples [13–15]. Among them, constructing *g*-C₃N₄-based heterojunction is an effective way to enhance the photocatalytic performance of *g*-C₃N₄ by improving the separation of charge carriers, such as *g*-C₃N₄/TiO₂ [16], *g*-C₃N₄/CdS [17], and *g*-C₃N₄/Ag₃PO₄ [18].

More recently, V–VI–VII ternary bismuth compounds BiOX (X = Cl, Br, I), featuring unique crystal structures consisting of $[Bi_2O_2]^{2+}$ slabs and interleaved halogen-ion layers, have attracted considerable attention because of their efficient photocatalytic activity [19–21]. In particular, BiOBr and BiOI can respond to visible light, thus harvesting high utilization efficiency in the solar spectrum. To further improve the photocatalytic reactivity, constructing heterostructures from BiOX without the introduction of foreign semiconductors is another new approach. So far, BiOX heterojunctions including BiOCl/BiOBr [22], BiOCl/BiOI [23],

✉ Bingkun Liu
liubk2015@zzuli.edu.cn

✉ Hengzhen Shi
shihz@zzuli.edu.cn

[1] School of Material and Chemical Engineering, Zhengzhou University of Light Industry, Zhengzhou 450002, People's Republic of China

[2] School of Food and Bioengineering, Zhengzhou University of Light Industry, Zhengzhou 450002, People's Republic of China

and BiOBr/BiOI [24] have been prepared by the one-pot method and demonstrated to have much higher photocatalytic activities than a single BiOX.

Based on above investigations, it would be interesting to develop g-C$_3$N$_4$/BiOX heterojunction photocatalysts by combining their advantages of each and further improve the charge separation at the same time. The groups of Zan have fabricated g-C$_3$N$_4$/BiOBr hybrid photocatalysts, which have been proved to show much higher VLD photocatalytic activity than pure g-C$_3$N$_4$ and BiOBr for rhodamine B degradation [25]. Xie et al. obtained g-C$_3$N$_4$/BiOI composite photocatalysts and demonstrated that their superior photocatalytic activity was attributed to the strong absorption in the visible region and low recombination rate of the electron–hole pairs by the formation of heterojunction [26]. However, to the best our knowledge, limited studies have reported the construction of g-C$_3$N$_4$ nanosheets/binary BiOX composites and their application in environmental disinfection.

In this work, we have synthesized g-C$_3$N$_4$/BiOI/BiOBr ternary heterojunction and the photocatalytic activity was evaluated by the degradation of methyl orange (MO) and inactivation of bacteria under visible light irradiation. The morphologies, structures, chemical compositions, optical properties, and photoactivity were characterized systematically. Moreover, the possible mechanism for the enhanced photocatalytic performance of g-C$_3$N$_4$/BiOI/BiOBr composites has also been discussed.

2 Experimental

2.1 Preparation of photocatalysts

g-C$_3$N$_4$ was synthesized by the thermal polycondensation of urea according to the literature [27]. Typically, urea (10 g) was placed into an alumina crucible with a cover, which was heated at a rate of 10 °C min^{-1} to reach 550 °C and was then calcined at this temperature for 2 h. After cooling to room temperature, the resulting product was collected and milled into a powder in an agate mortar for further use.

The pure BiOBr, BiOI and g-C$_3$N$_4$/BiOI/BiOBr composite were prepared by chemical precipitation. For the synthesis of g-C$_3$N$_4$/BiOI/BiOBr composite, 100 mg of g-C$_3$N$_4$ power were dispersed in 20 mL of deionized water, and then 1 mmol of Bi(NO$_3$)$_3$·5H$_2$O and 1 mmol of KBr were added to the above solution under vigorous stirring. Subsequently, 20 mL of an ethylene glycol (EG) solution containing various amount of KI was added dropwise. The precipitate was collected, washed repeatedly with water, and dried at 60 °C for 10 h. The as-synthesized samples were labeled as C$_3$N$_4$/BiOI/BiOBr-3%, C$_3$N$_4$/BiOI/BiOBr-5%, C$_3$N$_4$/BiOI/BiOBr-10%, C$_3$N$_4$/BiOI/BiOBr-20%, C$_3$N$_4$/BiOI/BiOBr-50% corresponding to the molar percentage of KI in the KI/KBr

mixed solution. Pure BiOBr (BiOI) was prepared by the same technique only using Bi(NO$_3$)$_3$·5H$_2$O and KBr (KI).

2.2 Characterizations

The crystal structure of the samples was characterized by X-ray diffraction (XRD) using a D8 advance X-ray diffractometer (Bruker Corporation) with Cu Kα radiation ($\lambda = 1.5405$ Å) at a scanning rate of 5° min^{-1}. X-ray photoelectron spectroscopy (XPS) spectra were collected with a monochromatic Al Kα X-ray source on an ESCALAB250 multitechnique X-ray photoelectron spectrometer. The morphology and lattice structure of the samples were measured by field emission scanning electron microscopy (FESEM, JSM-7001F, JEOL, Japan) and transmission electron microscopy (TEM, JEM-2100, JEOL, Japan). The UV–vis diffuse reflectance spectra (DRS) was recorded by UV–vis–NIR diffuse reflectance spectrum (Hitachi U-3900H, Japan). Steady state photoluminescence (PL) were recorded using F-7000 Fluorescence spectrometer (Hitachi 7000, Japan). The electron spin resonance (ESR) signals of radicals spin trapped by 5,5-dimethyl-l-pyrroline N-oxide (DMPO) were recorded by JEOL-JES-FA200 electron spin resonance spectrometry.

2.3 Photocatalytic degradation of MO

Photocatalytic activities of the prepared samples were evaluated for the degradation of methyl orange (MO, 10 mg L^{-1}) aqueous solution. Typically, 40 mL of aqueous solution of MO and 40 mg of photocatalysts were placed into a 100 mL beaker. Before light irradiation, the suspensions were magnetically stirred in the dark for 30 min to establish an adsorption–desorption equilibrium between the dye and the catalysts under ambient conditions. A 300 W Xe arc lamp through a UV-cutoff filter (≤ 400 nm) was used as the visible light source. At different irradiation intervals, an aliquot of the reaction solution was collected, centrifuged to remove the catalyst, and used to measure the concentration of MO by monitoring the absorbance with a UV–vis spectrophotometer (Hitachi U-3900H, Japan). To study the photocatalytic mechanism, trapping experiments were carried out to determine the main reactive species in the photocatalytic process. The experimental procedure was similar to the photocatalytic measurement except that the radical scavengers were added to the reaction system.

2.4 Photocatalytic bacterial inactivation

Escherichia coli (ATCC 15597) cells were cultivated in Luria–Bertani nutrient solution and followed by incubating on a BS-1E rotary shaker under 150 rpm and 37 °C for 12 h. After that, the bacterial cells were harvested by the centrifugation at 6000 rpm for 5 min at room temperature, then

washed twice a phosphate buffer solution (PBS, pH 7.0), and finally suspended with the same volume of the LB media in PBS. The final cell density was adjusted to about 1×10^9 colony forming unit (CFU) mL^{-1}. All solid/liquid materials had been autoclaved for 30 min at 121 °C before use.

A fixed concentration of 1 mg photocatalyst/mL *E. coli* suspension was used in the experiments. 10 mg photocatalyst with 9.9 mL buffer solution was first injected into a sterile 60 mm × 15 mm Petri dish and was dispersed ultrasonically for 10 min. Then, 0.1 mL *E. coli* suspensions were added into the Petri dish, so that the initial *E. coli* concentration used in the photoctalytic disinfection experiments was *ca.* 10^3 CFU mL^{-1}. A 300 W xenon lamp (HSX-F300, Beijing NBET Technology Co. Ltd., Beijing, China) was used for photocatalytic inactivation experiments, and the light with wavelengths below 400 nm was blocked by glass filters. The light intensity striking the cells were at *ca.* 10 mW cm^{-2}, as measured by a FZ-A optical Radiometer (Photoelectric Instrument Factory of Beijing Normal University, Beijing, China). At regular time intervals, 0.1 mL of the cell suspensions was withdrawn in sequence. Following the appropriate dilution with PBS buffer solution (pH ~ 7), aliquots of 0.1 mL were spread onto an agar medium plate. The plates were incubated at 37 °C for 24 h to determine the viable cell count. All analyses were conducted in triplicate.

3 Results and discussion

XRD was used to characterize the crystalline phases of the photocatalysts. Figure 1a shows the XRD patterns of the g-C$_3$N$_4$, BiOBr, BiOI and g-C$_3$N$_4$/BiOI/BiOBr composites. From the XRD patterns of g-C$_3$N$_4$, it can be seen that two typical diffraction peaks centered at 13.1° and 27.4°, which are characteristic of the (100) and (002) planes of g-C$_3$N$_4$. The intense peak at 27.4° is attributed to interlayer accumulation of conjugated aromatics, and the weak peak at 13.1° is related to in-plane arranged tri-s-triazine units. In the g-C$_3$N$_4$/BiOI/BiOBr-20% composite, all the XRD patterns could be well indexed to g-C$_3$N$_4$ and tetragonal phase of BiOBr (JCPDS 09-0393) and BiOI (JCPDS 10–0445). However, the (002) peak belonging to g-C$_3$N$_4$ decreases gradually and (100) peak almost disappears compared with the bare g-C$_3$N$_4$, which may be a result of high dispersion of g-C$_3$N$_4$ in the composite [28]. Meanwhile, it is found that the intensities of diffraction peaks of BiOI are strengthened gradually with increasing the BiOI amounts in the g-C$_3$N$_4$/BiOI/BiOBr, whereas those of BiOBr decrease simultaneously (Fig. 1b). The XRD results demonstrates the successful synthesis of the g-C$_3$N$_4$/BiOI/BiOBr composites.

The microstructures of g-C$_3$N$_4$, BiOBr, BiOI, and g-C$_3$N$_4$/BiOI/BiOBr composites were investigated by scanning electron microscopy (SEM), as shown in Fig. 2. It can

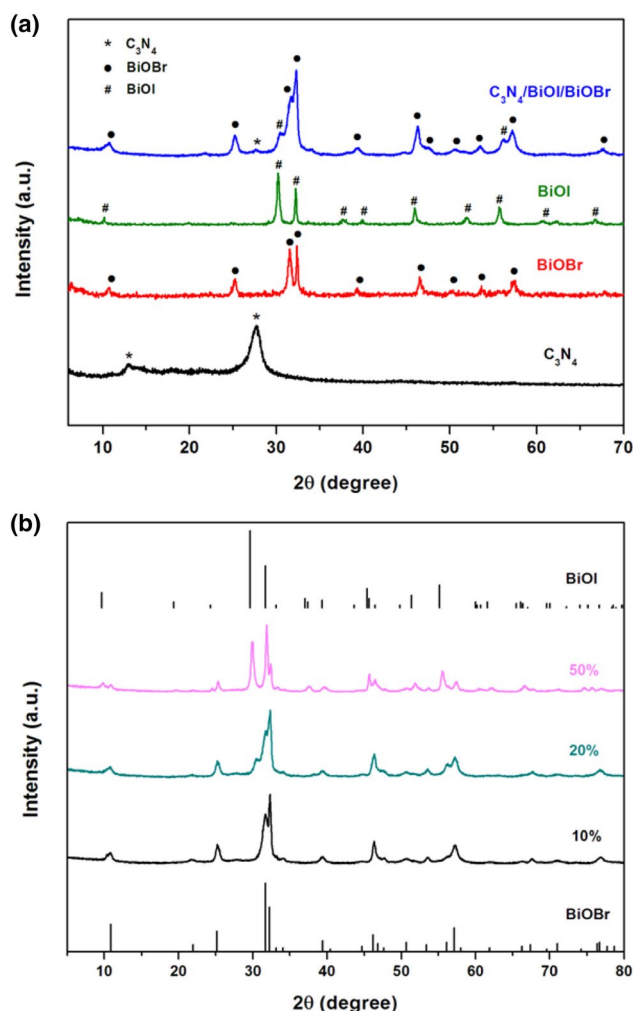**Fig. 1** XRD patterns of g-C$_3$N$_4$, BiOBr, BiOI and g-C$_3$N$_4$/BiOI/BiOBr composites with various amount of BiOI

be seen that the bare C$_3$N$_4$ sample is consist of large amounts of packing layers with different sizes of nanosheets (Fig. 2a). Figure 2b shows that the BiOI product consists of tiny nanoflakes with diameters in the range of 100–200 nm. In Fig. 2c, it could be clearly seen that the BiOI/BiOBr product exhibits the sphere-like structures with thin BiOI nanosheets on the large plate of BiOBr. For the g-C$_3$N$_4$/BiOI/BiOBr composite (Fig. 2d), it is found that curved g-C$_3$N$_4$ nanosheets was attached to the surface of the BiOI/BiOBr composite, which is favorable for the formation of heterojunctions.

A more detailed insight into the microstructure of the sample was given by TEM and HRTEM investigation. Figure 3a clearly shows that the BiOBr/BiOI microspheres are covered with g-C$_3$N$_4$ sheets, which was corresponding to the SEM results. The HRTEM image (Fig. 3b) of g-C$_3$N$_4$/BiOI/BiOBr sample show that there are two sets of lattice fringes with intervals of 0.274 and 0.266 nm that can be indexed to the (110) lattice plane of tetragonal BiOBr and

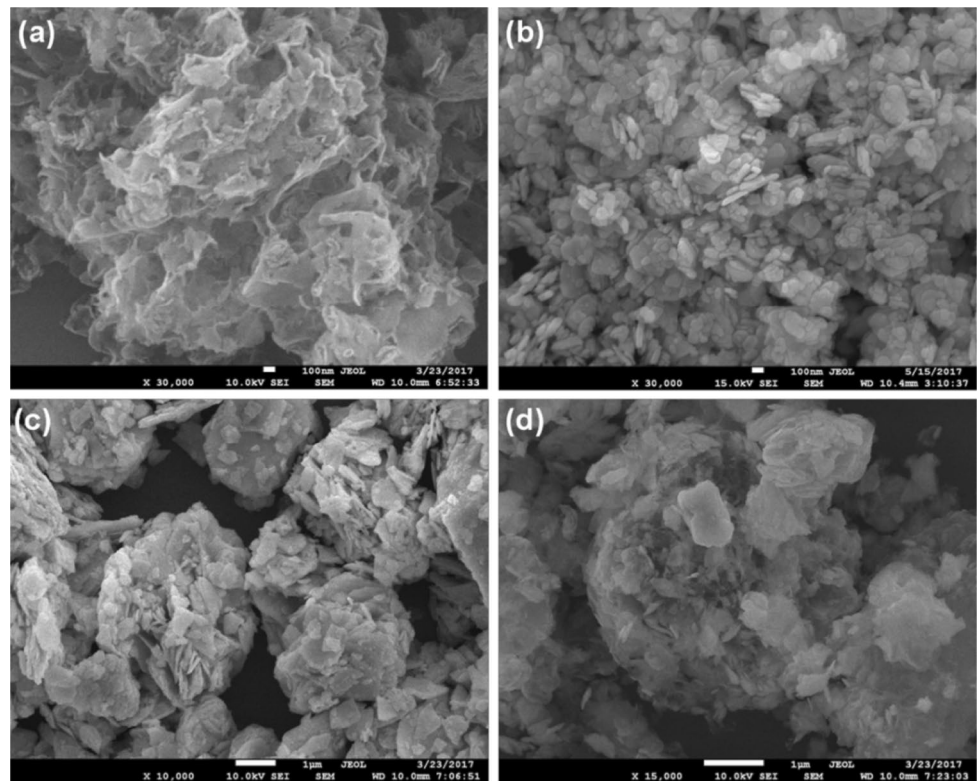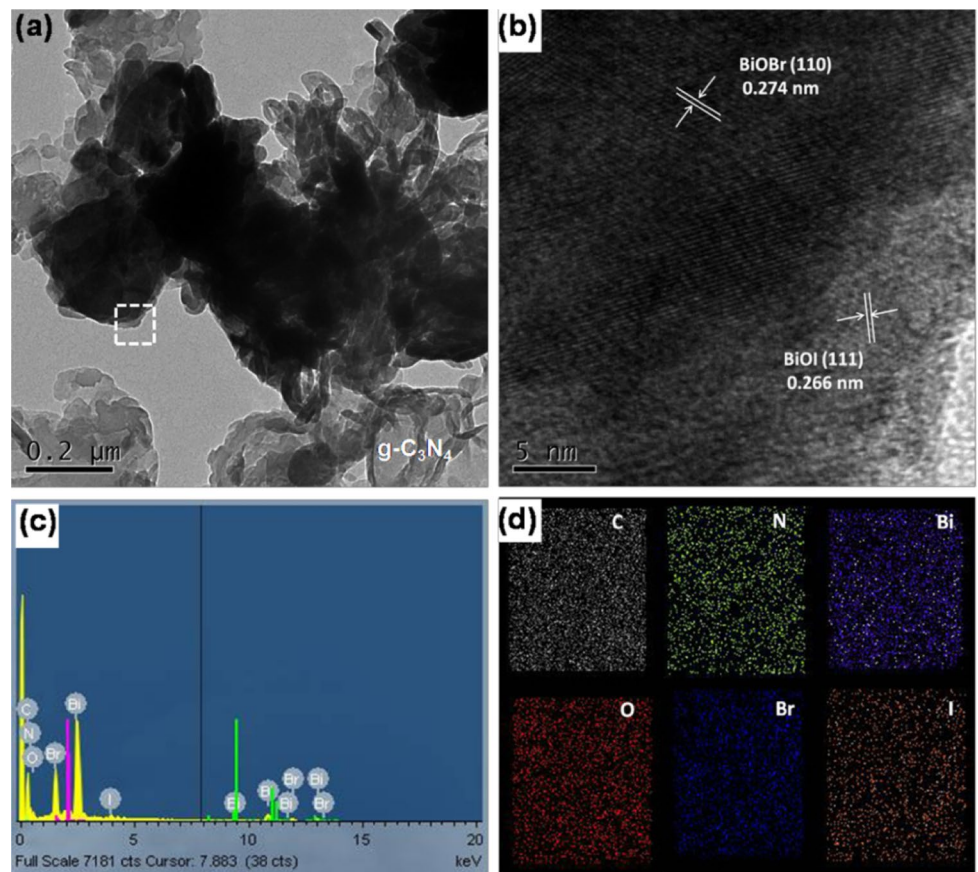**Fig. 2** FESEM images of **a** g-C$_3$N$_4$, **b** BiOI, **c** BiOI/BiOBr, and **d** g-C$_3$N$_4$/BiOI/BiOBr composite

Fig. 3 **a** TEM and **b** HRTEM images of g-C$_3$N$_4$/BiOI/BiOBr composite; **c** EDX and **d** elemental mapping images of the composite

the (111) crystal plane of BiOI, respectively. The corresponding EDS pattern and elemental mapping images of g-C_3N_4/BiOI/BiOBr heterostructure were shown in Fig. 3c, d. It clearly demonstrated the existence of C, N, Bi, O, Br and I in the composite, giving further proof that the formation of g-C_3N_4/BiOI/BiOBr heterostructures.

XPS measurements were performed to confirm the chemical compositions of g-C_3N_4/BiOI/BiOBr samples (Fig. 4). The survey XPS spectrum (Fig. 4a) clearly showed that the g-C_3N_4/

BiOI/BiOBr composite was composed of C, N, Bi, O, Br and I. High resolution spectra of C 1s, N 1s, Bi 4f, Br 3d and I 3d are shown in Fig. 4b–f. In the C 1s spectra (Fig. 4b), the peak located at 288.5 eV was assigned to the sp^2-hybridized carbon in the N=C–N_2 coordination, while the peak at 285.0 eV was ascribed to graphitic sites in the carbon nitride matrix C–C bonds [29, 30]. Figure 4c revealed the N 1 s spectra. The main peak at 399.2 eV was attributed to sp^2 hybridized aromatic nitrogen bonded to carbon atoms (C=N–C) [31]. The
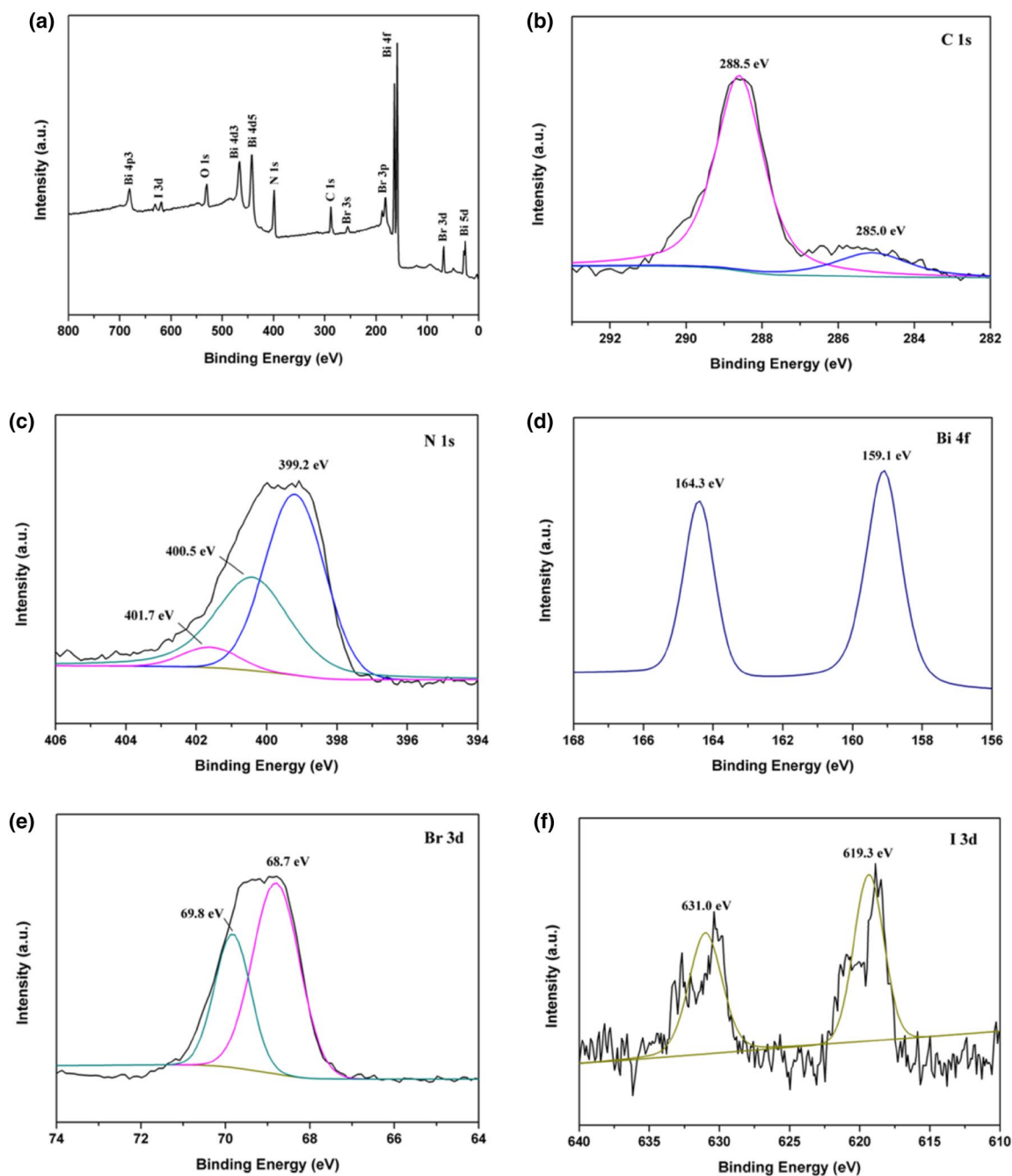

Fig. 4 XPS spectra of g-C_3N_4/BiOI/BiOBr composite: **a** survey; **b** C 1s; **c** N 1s; **d** Bi 4f; **e** Br 3d; **f** I 3d

two peaks at 400.5 and 401.7 eV corresponded to the tertiary nitrogen bonded to carbon atoms (N–(C)$_3$) and N–H groups, respectively [31, 32]. In Fig. 4d, the Bi 4f spectrum could be resolved into two spin orbit components at binding energies of 159.1 and 164.3 eV, which were assigned to Bi 4f$_{7/2}$ and Bi 4f$_{5/2}$ of Bi^{3+} in the g-C$_3$N$_4$/BiOI/BiOBr samples, respectively [29]. As for the high-resolution spectra of Br 3d (Fig. 4e), the peaks located at 68.7 and 69.8 eV are ascribed to Br 3d$_{5/2}$ and Br 3d$_{3/2}$ respectively, corresponding to Br$^-$ [33]. The I 3d peaks were located at 619.3 and 631.0 eV (Fig. 4f), which correspond to the I 3d$_{5/2}$ and I 3d$_{3/2}$ binding energies [34].

UV–vis diffuse reflectance spectra of the as-synthesized photocatalysts were displayed in Fig. 5a. It showed that g-C$_3$N$_4$ and BiOBr can absorb only light with wavelengths shorter than 450 nm, whereas the absorption edge of BiOI is approximately 670 nm. As for the g-C$_3$N$_4$/BiOI/BiOBr heterostructures, the absorption band edges were situated between those of BiOBr and BiOI, and gradually red-shifted with the increase of BiOI amount due to the strong visible light response of BiOI. The corresponding band gaps can be obtained from the equation $\alpha h\nu = A(h\nu - E_g)^{n/2}$, where α, $h\nu$, E_g, and A are the optical absorption coefficient, photonic energy, band gap, and proportionality constant, respectively [35]. Among them, n is determined by the type of optical transition of a semiconductor (n = 1 for direct transition and n = 4 for indirect transition). From the plot of $(\alpha h\nu)^{1/2}$ versus ($h\nu$) in Fig. 5b, the E_g of g-C$_3$N$_4$, BiOBr and BiOI were estimated to be 2.66, 2.88 and 1.84 eV, respectively. Because the heterostructure construction was closely related to the band potentials of the components, the edge positions of the conduction band (CB) and valence band (VB) of g-C$_3$N$_4$, BiOBr and BiOI were estimated by the expressions [36]:

$$E_{VB} = \chi - E_e + 0.5E_g$$

$$E_{CB} = E_{VB} - E_g$$

where E_{VB} and E_{CB} are the valence band (VB) and conduction band (CB) potentials, respectively; E_e (~ 4.5 eV) is the energy of free electrons on the hydrogen scale; E_g is the band gap; and χ is the electronegativity of the semiconductor. The E_{CB} values of g-C$_3$N$_4$, BiOBr and BiOI were calculated to − 1.11, 0.23 and 0.57 eV, respectively, and the E_{VB} values were estimated to be 1.55, 3.11 and 2.41 eV, respectively.

The photocatalytic activities of the as-synthesized samples were first evaluated by decomposing MO under visible light irradiation ($\lambda > 420$ nm). As shown in Fig. 6a, both BiOBr and BiOI exhibited weak photocatalytic activities that could only degrade MO by only 43.5 and 17.7% after 100 min of visible light irradiation, respectively. Nevertheless, the BiOI/BiOBr composite showed an obviously higher photocatalytic activity than those of BiOBr and BiOI. After the introduction of g-C$_3$N$_4$, the photocatalytic activity of g-C$_3$N$_4$/BiOI/BiOBr composite (C$_3$N$_4$/BiOI/BiOBr-10%) was further increased, which induced 99.7% degradation within 100 min. Figure 6b shows that there is a linear relationship between ln(C_0/C) and t, confirming that the photodegradation reaction is indeed pseudo-first-order. And the g-C$_3$N$_4$/BiOI/BiOBr composite showed the maximum rate constant of 0.0442 min^{-1}, which was almost 5.67, 7.62 and 23.26 times as high as those of individual g-C$_3$N$_4$ (0.0078 min^{-1}), BiOBr (0.0058 min^{-1}) and BiOI (0.0019 min^{-1}). In the meanwhile, it is found that the best photocatalytic activity of g-C$_3$N$_4$/BiOI/BiOBr was obtained when the optimum content of BiOI was located at 10% (Fig. 6c, d). On further increasing the contents of BiOI, the degradation rate showed an evident decrease. This is because the excess BiOI may reduce the heterojunction interface area and act as recombination centers of photo-induced electrons and holes [37].

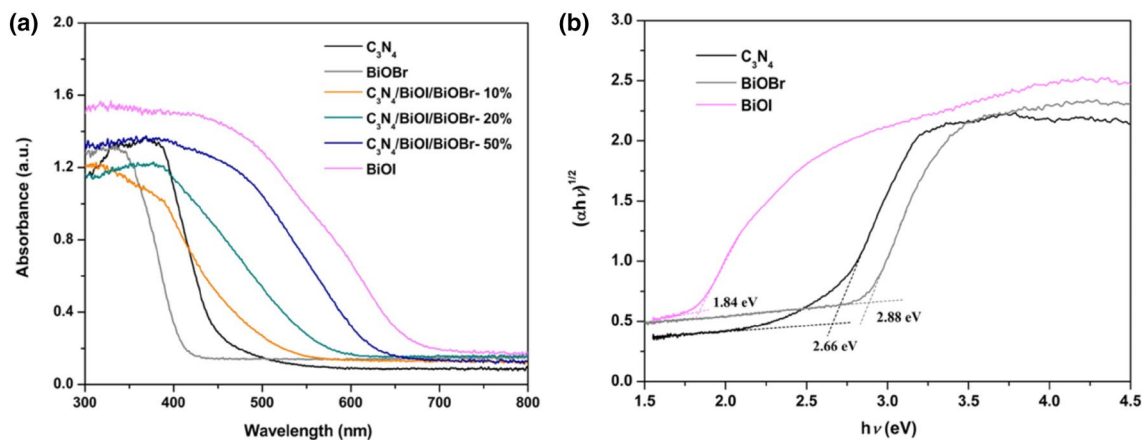The stability of the g-C$_3$N$_4$/BiOI/BiOBr composite was evaluated by several recycling runs. As shown in Fig. 7a,

Fig. 5 **a** UV–vis diffuse reflectance spectra of g-C$_3$N$_4$, BiOBr, BiOI and g-C$_3$N$_4$/BiOI/BiOBr composites; **b** the band gaps (E$_g$) of g-C$_3$N$_4$, BiOBr, BiOI samples with plots of $(\alpha h\nu)^{1/2}$ versus energy ($h\nu$)
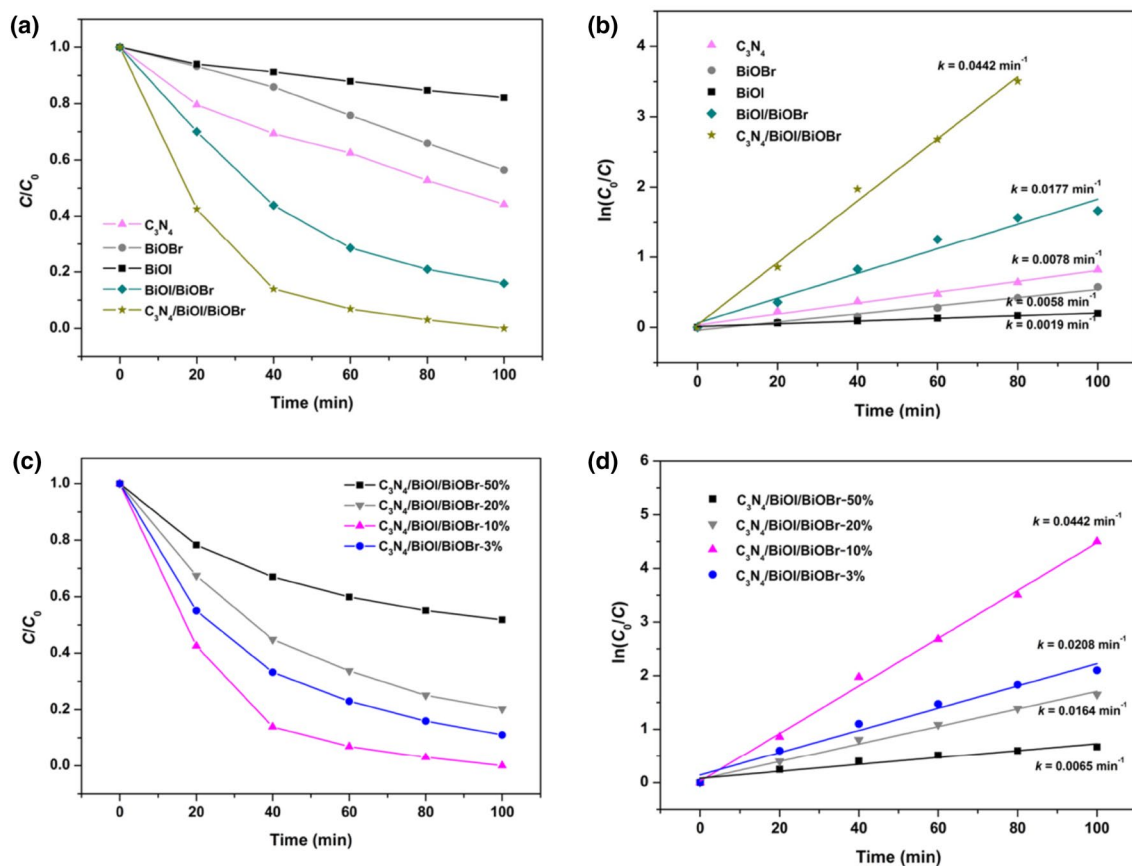
Fig. 6 **a** and **c** Photocatalytic degradation of MO by g-C$_3$N$_4$, BiOBr, BiOI and g-C$_3$N$_4$/BiOI/BiOBr composites under visible light irradiation; **b** and **d** linear transform ln(C_0/C) of the kinetic curves of MO degradation over different photocatalysts

after three recycles for the photodegradation of MO, photocatalytic performance of g-C$_3$N$_4$/BiOI/BiOBr maintained well, only with small loss of the activity. The structural and morphology stabilities of composite were also investigated by XRD and SEM after recycling experiments. As evident from Fig. 7b, c, no appreciable change was found from the XRD peaks and SEM image of the recycled samples. The result indicated that the crystal structure and morphology of the ternary hybrid material were not destroyed during the photocatalytic process, suggesting its good reusability and stability.

To investigate the predominant active species in the photodegradation process, we had carried out the control experiments with addition of scavenger for holes (h$^+$), ·OH and ·O$_2^-$ radical species. As presented in Fig. 8, about 99.7% of MO was removed after 100 min visible light irradiation in the g-C$_3$N$_4$/BiOI/BiOBr composite without any radical scavenger. When ethylenediamine tetra-acetic acid disodium salt (EDTA-2Na) or 4-hydroxy-2,2,6,6-tetramethylpiperidinyloxy (TEMPOL) was added, the photodegradation rates of MO were distinctly suppressed, confirming the important role of h$^+$ and ·O$_2^-$ in the degradation of MO. The addition

of isopropanol (IPA) causes little change in the photodegradation efficiency of MO, indicating ·OH is not a significant active species in the photocatalytic process. These experiments suggest that ·OH, ·O$_2^-$ and h$^+$ affect the degradation of MO, but h$^+$ and ·O$_2^-$ are the main reactive species in the degradation of MO.

To further confirm the reactive oxygen species (ROS) of g-C$_3$N$_4$/BiOI/BiOBr during the photocatalytic reaction, the ESR spin-trap technique was performed under dark and visible light irradiation. As shown in Fig. 9a, the characteristic peaks of DMPO-·O$_2^-$ are obviously observed, however no signals are found in dark. This result indicates that ·O$_2^-$ plays an important role in the photocatalytic reaction. From Fig. 9b, the characteristic peaks of DMPO-·OH can also be observed, but the signals of ·OH are relatively weak, implying that ·OH plays a less role in the photocatalytic reaction. The result is consistent with the trapping experiment of active species in the presence of different scavenger.

Photoluminescence emission spectra of different samples were performed to reveal the separation, transfer and recombination of the charge carriers on photocatalysts surface. Figure 10 shows the PL spectra of pure g-C$_3$N$_4$, BiOI/
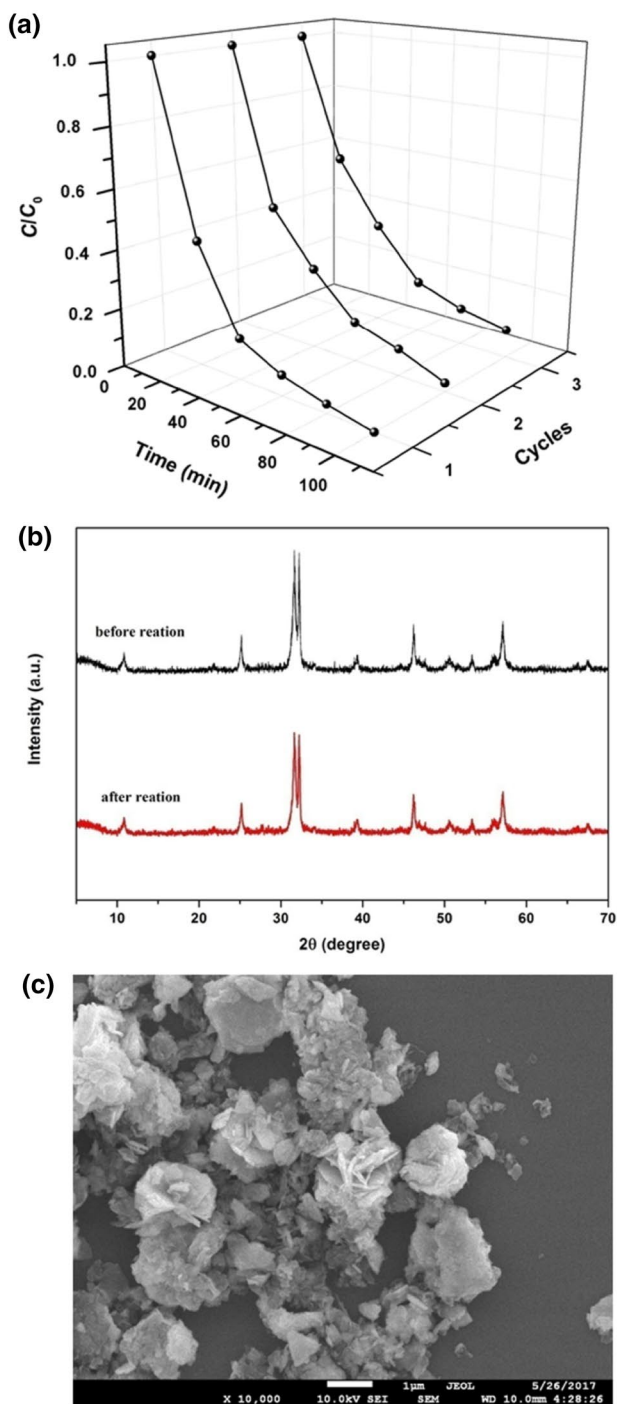
(a)

(b)

(c)

Fig. 7 a Recycled experiments for the MO degradation on g-C$_3$N$_4$/BiOI/BiOBr composite; **b** XRD patterns of the composite before and after three recycle photocatalytic degradation process; **c** FESEM image of g-C$_3$N$_4$/BiOI/BiOBr composite after the cycling photocatalytic experiments
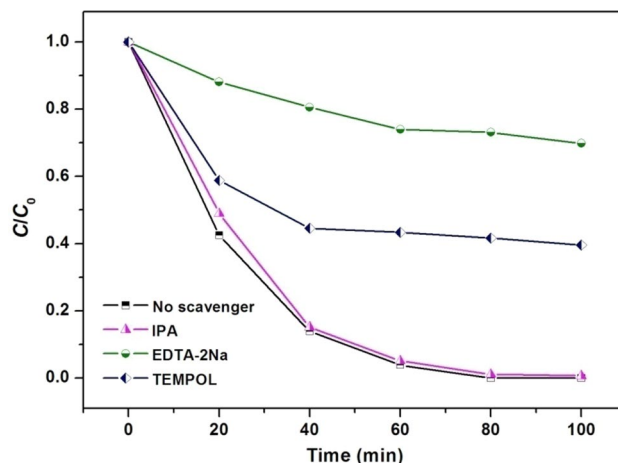

Fig. 8 Photocatalytic degradation of MO by g-C$_3$N$_4$/BiOI/BiOBr composite with different scavengers

the heterojunction effect in the composite contributes to the effective electron–hole pair separation, which could be a reason for the g-C$_3$N$_4$/BiOI/BiOBr heterostructures showing superior photocatalytic activity under visible light.

The antibacterial activity of various photocatalysts is evaluated by visible light induced photocatalytic disinfection of *E. coli*, a common Gram-negative bacterium. From the Fig. 11a, b, it indicated that pure BiOBr and BiOI showed weak bacteriostatic activity, and only about 29.4 and 34.2% of *E. coli* were killed after 5 h of visible light irradiation. As for the pure g-C$_3$N$_4$ (Fig. 11c), it achieves 36.2 and 83.7% of *E. coli* inactivation within 3 and 5 h, respectively. More interesting, the photocatalytic antibacterial activity of g-C$_3$N$_4$/BiOI/BiOBr composite is obviously enhanced as compared to individual photocatalysts. With the visible light irradiation for more than 3 h, almost all of *E. coli* cells are killed, as shown in Fig. 11d, e. The results are in good agreement with the photocatalytic degradation of MO.

According to the calculated results, the conduction band (CB) and valence band (VB) potentials of g-C$_3$N$_4$ are about − 1.11 and 1.55 eV. The CB bottom of BiOI (0.57 eV) lies below that of BiOBr (0.23 eV), while the VB top of BiOI (2.41 eV) is higher than that of BiOBr (3.11 eV). The previous literature reported that the electrons on the VB of BiOI could be excited to a higher potential edge (− 0.65 eV), while that of BiOBr was excited to 0.10 eV [38]. Thus, there are two possible charge separation ways for g-C$_3$N$_4$/BiOI/BiOBr composite (Fig. 12). In detail, one is the traditional double-transfer mechanism and the other is Z-scheme mechanism. As shown in Fig. 12a, the electrons in the CB of g-C$_3$N$_4$ will migrate to the CB of BiOI and then transfer to the CB of BiOBr according to the double-transfer mechanism. Meanwhile, the photo-excited holes in the VB of BiOBr will transfer to the VB of BiOI and g-C$_3$N$_4$. As a
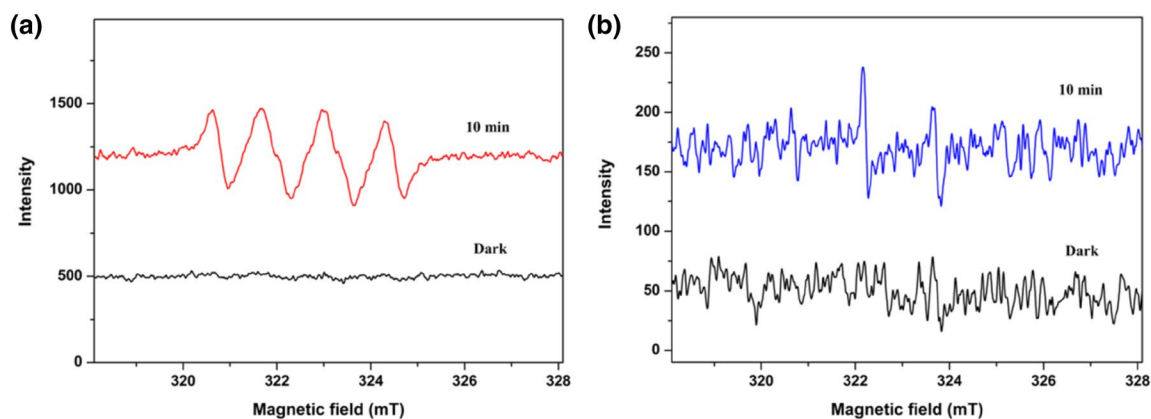
BiOBr and g-C$_3$N$_4$/BiOI/BiOBr samples under excitation of 325 nm light irradiation. Compared with g-C$_3$N$_4$ and BiOI/BiOBr, the ternary hybrid materials of g-C$_3$N$_4$/BiOI/BiOBr was found to have the weaker PL intensity, indicating that

Fig. 9 ESR spectra with g-C_3N_4/BiOI/BiOBr sample under visible light irradiation for **a** DMPO-·O_2^- in a methanol dispersion and **b** DMPO-·OH in an aqueous dispersion
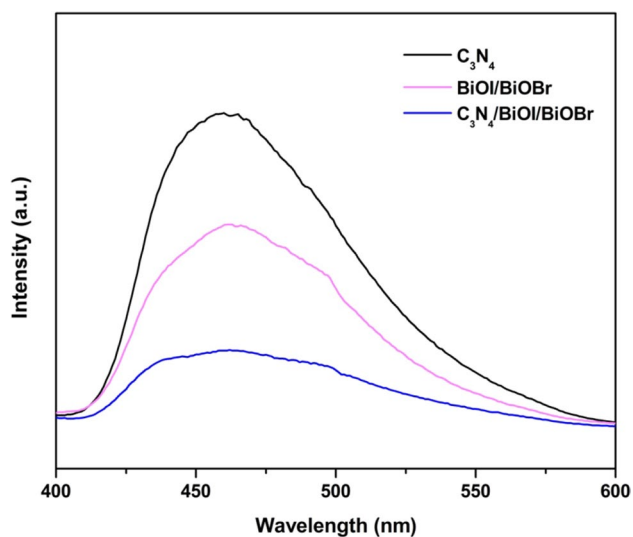
Fig. 10 Photoluminescence spectra of g-C_3N_4, BiOI/BiOBr and g-C_3N_4/BiOI/BiOBr composite

Fig. 11 a–d Photos of *E. coli* colonies on an agar plate before and after visible light irradiation using BiOBr, BiOI, g-C_3N_4 and g-C_3N_4/BiOI/BiOBr composite; **e** antibacterial activities of the prepared photocatalysts against *E. coli* in the dark and under visible light irradiation

result, the accumulated electrons in the CB of BiOBr cannot reduce O_2 to ·O_2^- and the holes in the VB of g-C_3N_4 could not oxidize H_2O to generate ·OH [39, 40]. However, the trapping experiment and ESR results indicated that ·O_2^-, h^+ and ·OH are the reactive oxygen species in the photocatalytic process. Therefore, the separation and transfer process of the photogenerated electron–hole charges should not follow the common heterojunction process in Fig. 12a.

Based on the above discussion and the experimental results, a possible direct solid-state Z-scheme mechanism was proposed. As schematized in Fig. 12b, g-C_3N_4, BiOI and BiOBr can produce photoinduced electron–hole pairs under visible light irradiation. Then, the photoinduced electrons in the CB of BiOBr would transfer and recombine with the holes in the VB of BiOI [41]. As a result, the electrons
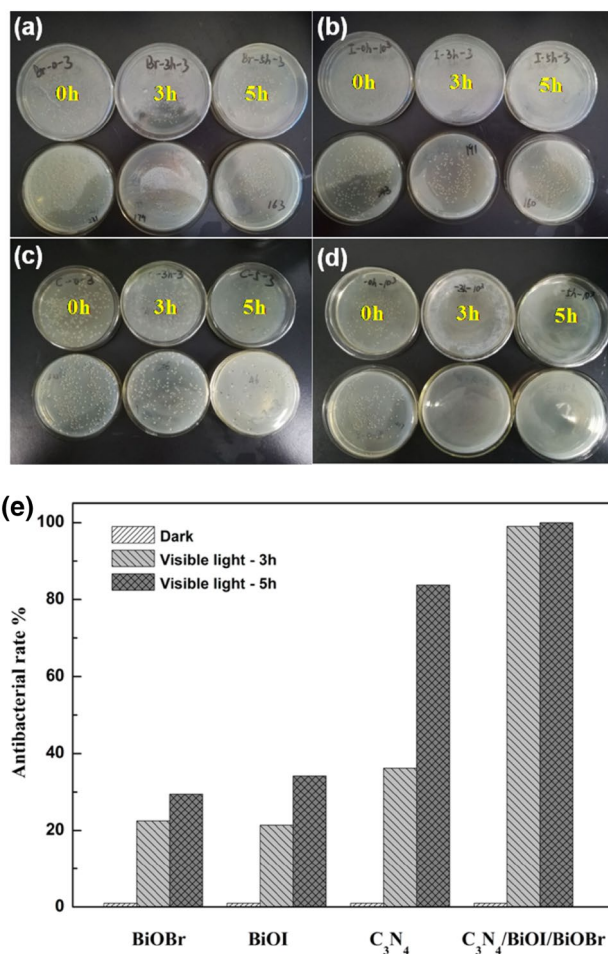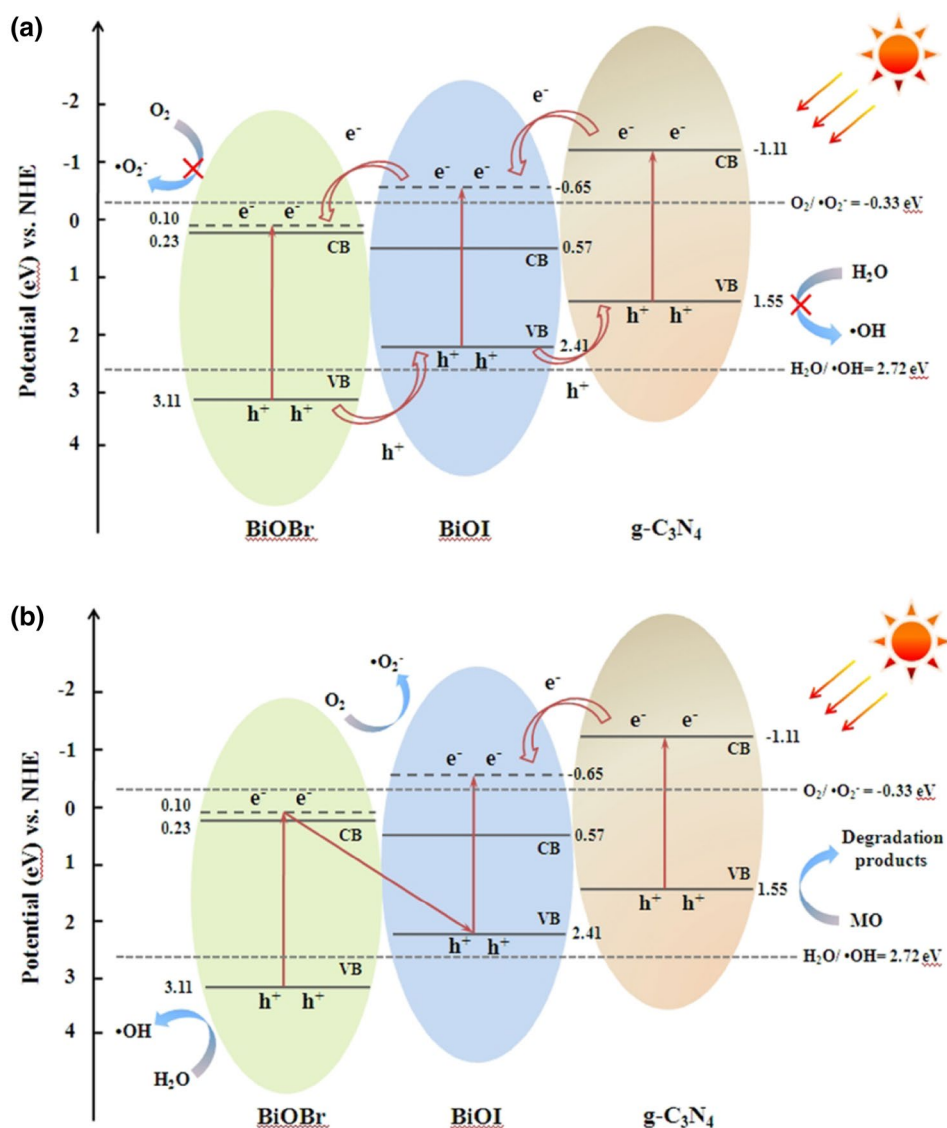
Fig. 12 Schematic illustration of the proposed photocatalytic mechanisms over g-C$_3$N$_4$/BiOI/BiOBr composite under visible light irradiation

in the CB of BiOI can reduce O$_2$ to ·O$_2^-$ due to their more negative potential. Simultaneously, the holes in the VB of BiOBr have enough energy to oxidize H$_2$O to form ·OH. The holes in the VB of g-C$_3$N$_4$ are also available to degrade organic pollutants. Thus a model based on the Z-scheme system is favorable for the production of the ·O$_2^-$, ·OH and h$^+$ reactive species.

4 Conclusions

In this paper, g-C$_3$N$_4$/BiOI/BiOBr heterostructure were successfully prepared by a simple deposition precipitation method. The ternary composites display better photocatalytic activity than single photocatalyst for the degradation of MO and inactivation of *E. coli* under visible light irradiation. The enhanced photocatalytic performances can be ascribed to improved visible light absorption and effective separation of the photo-induced charge carriers in the g-C$_3$N$_4$/BiOI/BiOBr composite. The radical trapping experiment and ESR analysis confirmed that the active species ·O$_2^-$, h$^+$ and ·OH are the reactive oxygen species in the photocatalytic process. This work could provide a new insight to the development of composite photocatalysts for environmental application.

References

1. M.N. Chong, B. Jin, C.W.K. Chow, C. Saint, Water Res. **44**, 2997–3027 (2010)
2. L. Liu, J. Liu, D.D. Sun, Catal. Sci. Technol. **2**, 2525–2532 (2012)
3. J. Xu, Z. Wang, Y. Zhu, ACS Appl. Mater. Interfaces **9**, 27727–27735 (2017)
4. M. Pelaez, N.T. Nolan, S.C. Pillai, M.K. Seery, P. Falaras, A.G. Kontos, P.S.M. Dunlop, J.W.J. Hamilton, J.A. Byrne, K. O'Shea, M.H. Entezari, D.D. Dionysiou, Appl. Catal. B **125**, 331–349 (2012)
5. Z. Xing, J. Zhang, J. Cui, J. Yin, T. Zhao, J. Kuang, Z. Xiu, N. Wan, W. Zhou, Appl. Catal. B **225**, 452–467 (2018)
6. Y. Ma, X. Wang, Y. Jia, X. Chen, H. Han, C. Li, Chem. Rev. **114**, 9987–10043 (2014)
7. X. Wang, K. Maeda, A. Thomas, K. Takanabe, G. Xin, J.M. Carlsson, K. Domen, M. Antonietti, Nat. Mater. **8**, 76–80 (2008)
8. W.-J. Ong, L.-L. Tan, Y.H. Ng, S.-T. Yong, S.-P. Chai, Chem. Rev. **116**, 7159–7329 (2016)
9. G. Zhang, G. Li, Z.A. Lan, L. Lin, A. Savateev, T. Heil, S. Zafeiratos, X. Wang, M. Antonietti, Angew. Chem. Int. Ed. **56**, 13445–13449 (2017)
10. J. Xu, H.-T. Wu, X. Wang, B. Xue, Y.-X. Li, Y. Cao, Phys. Chem. Chem. Phys. **15**, 4510–4517 (2013)
11. S. Tonda, S. Kumar, S. Kandula, V. Shanker, J. Mater. Chem. A **2**, 6772–6780 (2014)
12. G. Liu, P. Niu, C. Sun, S.C. Smith, Z. Chen, G.Q. Lu, H.-M. Cheng, J. Am. Chem. Soc. **132**, 11642–11648 (2010)
13. Z. Zhao, Y. Sun, F. Dong, Nanoscale **7**, 15–37 (2015)
14. J. Fu, J. Yu, C. Jiang, B. Cheng, Adv. Energy Mater. **8**, 1701503 (2018)
15. F. Ding, D. Yang, Z. Tong, Y. Nan, Y. Wang, X. Zou, Z. Jiang, Environ. Sci. **4**, 1455–1469 (2017)
16. K. Sridharan, E. Jang, T.J. Park, Appl. Catal. B **142–143**, 718–728 (2013)
17. F. Jiang, T. Yan, H. Chen, A. Sun, C. Xu, X. Wang, Appl. Surf. Sci. **295**, 164–172 (2014)
18. S. Kumar, T. Surendar, A. Baruah, V. Shanker, J. Mater. Chem. A **1**, 5333–5340 (2013)
19. X. Zhang, Z. Ai, F. Jia, L. Zhang, J. Phys. Chem. C **112**, 747–753 (2008)
20. H. An, Y. Du, T. Wang, C. Wang, W. Hao, J. Zhang, Rare Met. **27**, 243–250 (2008)
21. L. Ye, Y. Su, X. Jin, H. Xie, C. Zhang, Environ. Sci. **1**, 90–112 (2014)
22. S. Zhang, J. Yang, Ind. Eng. Chem. Res. **54**, 9913–9919 (2015)
23. T.B. Li, G. Chen, C. Zhou, Z.Y. Shen, R.C. Jin, J.X. Sun, Dalton Trans. **40**, 6751–6758 (2011)
24. H. Huang, X. Han, X. Li, S. Wang, P.K. Chu, Y. Zhang, ACS Appl. Mater. Interfaces **7**, 482–492 (2015)
25. L. Ye, J. Liu, Z. Jiang, T. Peng, L. Zan, Appl. Catal. B **142–143**, 1–7 (2013)
26. D. Jiang, L. Chen, J. Zhu, M. Chen, W. Shi, J. Xie, Dalton Trans. **42**, 15726–15734 (2013)
27. Y. Zhang, J. Liu, G. Wu, W. Chen, Nanoscale **4**, 5300–5303 (2012)
28. S.M. Aghdam, M. Haghighi, S. Allahyari, L. Yosefi, J. Photochem. Photobiol. A **338**, 201–212 (2017)
29. Z. Yang, J. Li, F. Cheng, Z. Chen, X. Dong, J. Alloys Compd. **634**, 215–222 (2015)
30. F. Dong, Z. Zhao, T. Xiong, Z. Ni, W. Zhang, Y. Sun, W.-K. Ho, ACS Appl. Mater. Interfaces **5**, 11392–11401 (2013)
31. Y. Li, Y. Li, S. Ma, P. Wang, Q. Hou, J. Han, S. Zhan, J. Hazard. Mater. **338**, 33–46 (2017)
32. G. Li, X. Nie, J. Chen, Q. Jiang, T. An, P.K. Wong, H. Zhang, H. Zhao, H. Yamashita, Water Res. **86**, 17–24 (2015)
33. D. Wu, S. Yue, W. Wang, T. An, G. Li, H.Y. Yip, H. Zhao, P.K. Wong, Appl. Catal. B **192**, 35–45 (2016)
34. J. Jiang, X. Zhang, P. Sun, L. Zhang, J. Phys. Chem. C **115**, 20555–20564 (2011)
35. M.A. Butler, J. Appl. Phys. **48**, 1914–1920 (1977)
36. M.A. Butler, D.S. Ginley, J. Electrochem. Soc. **125**, 228–232 (1978)
37. J. Cao, X. Li, H. Lin, S. Chen, X. Fu, J. Hazard. Mater. **239–240**, 316–324 (2012)
38. J. Cao, B. Xu, B. Luo, H. Lin, S. Chen, Catal. Commun. **13**, 63–68 (2011)
39. J. Huang, W. Ho, X. Wang, Chem. Commun. **50**, 4338–4340 (2014)
40. Y. Bao, K. Chen, Appl. Surf. Sci. **437**, 51–61 (2018)
41. D. Yuan, L. Huang, Y. Li, Y. Xu, H. Xu, S. Huang, J. Yan, M. He, H. Li, RSC Adv. **6**, 41204–41213 (2016)